

A study of the low-mass X-ray binary dip sources XB 1916–053, XB 1323–619, X 1624–490 and 4U 1746–371 observed with INTEGRAL

Ş. Balman^{1,2}

ABSTRACT

We detect dipping activity/modulations in the light curve of the four LMXBs in the 3–10 keV and 20–40 keV energy ranges. The spectral parameters derived from the fits to the INTEGRAL data are consistent with hot coronal structures in these systems where we find a range of plasma temperatures 3.0–224.9 keV. The unabsorbed X-ray to soft Gamma-ray flux between 4–200 keV are 5.9×10^{-10} erg s⁻¹ cm⁻² for XB 1916–053, 3.3×10^{-10} erg s⁻¹ cm⁻² for XB 1323–619, 21.6×10^{-10} erg s⁻¹ cm⁻² for X 1624–490 and 11.0×10^{-10} erg s⁻¹ cm⁻² for 4U 1746–371. The optical depth to Compton scattering, τ , varies in a range 4.4–0.002 consistent with electron densities $n_e < 1.4 \times 10^{15}$ cm⁻³. In general, we find no significant difference in the dip and non-dip spectra in the ISGRI energy range (above 20 keV) for all the four sources. We only detect absorption differences between dipping and non-dipping intervals for XB 1916–053 and X 1624–490 in the JEM-X energy range. Fits in the 4–200 keV range including an additional photo-ionized absorber model for the two sources show that XB 1916–053 has the highest ionized absorber among the two.

Subject headings: X-ray: binaries – accretion, accretion disks – Radiation Mechanisms: general – X-rays: individual: XB 1916–053, XB 1323–619, X 1624–490, 4U 1746–371

1. INTRODUCTION

Some galactic low-mass X-ray binaries (LMXBs) show periodic dips in their X-ray intensity. The dipping behaviour repeats with the orbital period of the systems and is caused by periodic obscuration of the X-ray emitting region by a structure located in the outer regions of a disk particularly believed to be the impact region of the accretion flow from the companion star (White & Swank 1982). The depth, duration and spectral properties of the dips vary according to the source and binary phase. There are about 10 members (some candidates) of these systems. The 1–10 keV spectra of most of the dip sources become harder during dipping. This change is accepted to be

¹Middle East Technical University, Physics Department, Inonu Bulvari, 356531, Ankara, Turkiye; solen@astroa.physics.metu.edu.tr

²Astrophysics Missions Division, Research and Scientific Support Department of ESA, ESTEC, Postbus 299, NL-2200 AG Noordwijk, The Netherlands

inconsistent with an increase in the photo-electric absorption by cool material since an excess of low-energy photons is also observed to be present in some of the systems (e.g., EXO 0748–676: Cottam et al. 2001).

Several approaches is used to model this spectral evolution (persistent–non-dip to dip spectra). The first approach is the "absorbed plus unabsorbed" (e.g., Parmar et al. 1986; Courvoisier et al. 1986; Smale et al. 1992) where the persistent (non-dipping) spectral shape is used to model spectra from dipping intervals. The spectral evolution during dipping is accounted for by large increases in the column density of the absorbed component, and decreases of the normalization of the unabsorbed component. The latter decrease is attributed to electron scattering in the absorber. The changing normalization was difficult to justify and thus, a more complete and updated version of the model above was adopted as the "progressive covering", or by name "complex continuum" approach (e.g., Church et al. 1997; Barnard et al. 2001), where the X-ray emission is assumed to originate from a point-like blackbody (the neutron star), or disk-blackbody component, together with an extended power-law component. This approach uses a model where the extended component is partially and progressively covered in time by an opaque absorber to explain the spectral changes during dipping episodes. In such episodes, the blackbody component is also absorbed.

More recently, the improved sensitivity and spectral resolution of XMM-Newton, *Chandra* and *Suzaku* have aided the detection of narrow absorption features from highly ionized Fe (the Fe XXV and Fe XXVI lines) and other metals from several X-ray binaries (Lee et al. 2002; Sidoli et al. 2001, 2002; Ueda et al. 2004; Parmar et al. 2002; Boirin et al. 2004; Juett & Chakrabarty 2006; Miller et al. 2004, 2006; Kubota et al. 2007; Iaria et al. 2007, 2006; Díaz Trigo et al. 2009). A thorough analysis of XMM-Newton data of dipping LMXBs (Boirin et al. 2005; Díaz Trigo et al. 2006) have recovered highly ionized Fe absorption features from these systems and demonstrated that modeling the changes in both the observed X-ray absorption lines and continuum seen during the dips and persistent emission can be explained by an increase in the column density and a decrease in the amount of ionization of a highly photoionized absorbing plasma.

The dipping LMXB sources have been well studied with the RXTE and Beppo-Sax missions in an energy range out to ~ 20 keV (Parmar et al. 1999; Bałucińska-Church et al. 2004; Barnard et al. 2001; Bałucińska-Church et al. 1999; Narita et al. 2003a; Church et al. 1998; Bałucińska-Church et al. 2000; Smale et al. 2001). Though both missions have harder energy range detectors (RXTE–HEXTE detector and Beppo-Sax–PDS detector), the diminishing sensitivity and short observation durations have not yielded effective analysis of light curves and spectra above 20 keV. This in the end yields spectral parameters that vary according to the detector and mission regardless of intrinsic source variability. The ESA's γ -ray observatory INTEGRAL will allow for the determination of the widest energy band observed for dipping LMXB sources with the highest possible sensitivity above 20 keV. The energy range of the data (~ 15 –500 keV) provided by the INTEGRAL observatory ISGRI detector supported by the lower energy JEM-X data should reveal the best parameters at high S/N that describe the broad-band spectrum of the dipping LMXBs together with the effects of scattering at high energies. Furthermore, we extend the investigation of the role

of photo-ionized plasmas via application of warmabsorber models in dipping LMXBs beyond the 10 keV upper energy limit of previous studies using data from INTEGRAL observatory.

In this paper, we derive light curves and spectra for four dipping LMXB systems, XB 1916–053, XB 1323–619, 4U 1746–371, and X 1624–490. We discuss the dipping activity visible in the light curves and describe the broad-band time-averaged spectral characteristics of each source. We compare the dip and persistent (non-dip) spectra of the sources. We discuss and elaborate on the results of the spectral fits and compare these with previous findings in the light of the present physical models of accretion disk coronae and photo-ionized absorbers.

1.1. Source properties

The properties of the four dip sources studied here (XB 1916–053, XB 1323–619, 4U 1746–371 and X 1624–490) are summarized in Table 1.

XB 1916–053 is the dip source with the shortest period known of 0.83 hr (Walter et al. 1982). The presence of dips and the lack of X-ray eclipses from the companion star indicate that the system is viewed at an inclination angle, i , of $\sim 60\text{--}80^\circ$ (Frank et al. 1987; Smale et al. 1988). By combining archival and R-XTE observations, Chou et al. (2001) were able to derive a precise dip recurrence interval of 0.83351411(25) hr. The optical counterpart shows a modulation with a period 1% longer (Callanan et al. 1995, and references therein). The presence of superhumps (Schmidtke 1988; Retter et al. 2002) have been proposed to account for this difference. XB 1916–053 has shown a 270 Hz highly coherent oscillation during a type I X-ray burst indicating that the neutron star is spinning rapidly with a period of 3.7 ms (Galloway et al. 2001). The source has also shown quasi-periodic oscillations (QPOs) at various frequencies ranging from ~ 0.2 to 1300 Hz (Boirin et al. 2000). The BeppoSAX 0.2–200 keV non-dip (or "persistent") spectrum may be modeled using an absorbed blackbody with a temperature, kT , of 1.62 ± 0.05 keV and an absorbed cut-off power-law with a photon index, Γ , of 1.61 ± 0.01 and a relatively high cut-off energy, E_{cut} , of 80 ± 10 keV (Church et al. 1998). Narrow absorption features due to Fe XXV and FeXXVI in the XMM-Newton spectrum were discovered by Boirin et al. (2004) which was interpreted as the existence of a warm absorber in the system. On the other hand, for XB 1916–053 progressive covering gives a good description of the spectral evolution in dipping from both ASCA and SAX observations, as well (Church et al. 1997, 1998).

XB 1323–619 exhibits X-ray bursts and irregular intensity dips that repeat every 2.94 hr. The source was first detected by *Uhuru* and *Ariel V* (Forman et al. 1978; Warwick et al. 1981) and the dips and bursts were discovered using EXOSAT (van der Klis et al. 1985; Parmar et al. 1989a). During the dips, which typically last for 30% of the orbital cycle, the 1–8 keV intensity varies irregularly with a minimum of $\sim 50\%$ of the average value outside of the dips. The presence of periodic dips and the absence of X-ray eclipses indicates that the source is also viewed at $i = 60\text{--}80^\circ$ (Frank et al. 1987). The dip recurrence interval is not so precisely known, with the best

measurement being that of Bałucińska-Church et al. (1999) of 2.94(2) hr. The source exhibits ~ 1 Hz QPOs which have been attributed to a disk instability (Jonker et al. 1999). The BeppoSAX 1.0–150 keV spectrum of the XB 1323–619 persistent emission can be modeled by a cutoff power-law with $\Gamma = 1.48 \pm 0.01$ and $E_{\text{cut}} = 44.1^{+5.1}_{-4.4}$ keV together with a blackbody with $kT = 1.77 \pm 0.25$ keV (Bałucińska-Church et al. 1999). Boirin et al. (2005) examined the changes in the properties of the Fe XXV and Fe XXVI absorption features during persistent and dipping intervals. They found evidence for the presence of less-ionized material in the line of sight during dips supporting the warm absorber scenario. Church et al. (2005) also explains the XMM observations of this source using the progressive covering model where they attribute the absorption features to an existing accretion disk corona.

4U 1746–371 is located in the globular cluster NGC 6441. The source exhibited 3 apparently energy independent intensity dips separated by 5.0(5) hr, as well as flaring and bursting behavior (Parmar et al. 1989b). The dips are shallow (25% of the continuum intensity) and largely energy independent in the usable energy range of the R-XTE Proportional Counter Array (2.1–16 keV) (Bałucińska-Church et al. 2004). The best estimate of the dip period is 5.16 ± 0.01 hr (Bałucińska-Church et al. 2004). The BeppoSAX 0.3–30 keV spectrum of 4U 1746–371 is unusually soft and is dominated by a disk blackbody with $kT = 2.82 \pm 0.04$ keV, together with a cutoff power-law with $\Gamma = -0.32 \pm 0.80$ and E_{cut} of 0.90 ± 0.26 keV (Parmar et al. 1999).

X 1624–490 exhibits irregular dips in X-ray intensity that repeat every orbital cycle of 21 hr (Jones & Watson 1989). This long orbital period means that as well as being the most luminous dip source, X 1624–490 also has the largest stellar separation and is often referred to as the "Big Dipper". The X 1624–490 X-ray light curve exhibits prominent flares at energies > 15 keV and dipping is evident at energies up to 6 keV (Smale et al. 2001). These authors determine a dip recurrence interval of 20.8778(3) hr. In contrast to the other dip sources studied, no X-ray bursts have been observed from X 1624–490 (e.g., Bałucińska-Church et al. 2000; Smale et al. 2001). The 1–100 keV BeppoSAX persistent spectrum of X 1624–490 may be modelled using a blackbody with $kT = 1.31 \pm 0.07$ keV and a cutoff power-law with $\Gamma = 2.0^{+0.5}_{-0.7}$ and an E_{cut} of ~ 12 keV (Bałucińska-Church et al. 2000). Narrow absorption line features identified with Fe XXV and Fe XXVI were discovered from X 1624–490 using XMM-Newton by Parmar et al. (2002).

2. Observations and data reduction

The INTEGRAL (Winkler et al. 2003) payload consists of two γ -ray instruments, one optimized for 15 keV to 10 MeV high-resolution imaging (IBIS; Ubertini et al. 2003) and the other for 18 keV to 8 MeV high-resolution spectroscopy (SPI; Vedrenne et al. 2003). IBIS provides an angular resolution of $12'$ full-width at half-maximum (FWHM), a fully coded field of view (FOV) of $8^{\circ}3 \times 8^{\circ}$, and a FWHM energy resolution, $E/\Delta E$, of 12 at 100 keV. SPI provides an angular resolution of $2^{\circ}5$ FWHM, a fully coded hexagonal FOV of $13^{\circ}2 \times 13^{\circ}2$ and a FWHM $E/\Delta E$ of 430 at 1.3 MeV. The extremely broad energy range of IBIS is covered by two separate detector

arrays, ISGRI (15–1000 keV) and PICsIT (0.175–10 MeV). In addition, the payload includes X-ray (JEM-X; 3–35 keV; Lund et al. 2003) and optical (OMC; V-band; Mas-Hesse et al. 2003) monitors. JEM-X has a fully coded FOV of 4° diameter and an angular resolution of 3' FWHM. All the instruments are co-aligned and operated simultaneously. The data used here were obtained from the INTEGRAL Science Data Centre (ISDC; Courvoisier et al. 2003) archive. For this study, all publically available pointings between January 2003 and November 2004 (revolutions 30 to 250) where one of the selected sources was within 10° of the centre of the FOVs were included. Table 2 is an observation log.

For this study, data from the ISGRI and JEM-X instruments were used due to their good sensitivity and broad energy coverage and processed using the Off-line Scientific Analysis (OSA 5.1) software provided by the ISDC. This includes pipelines for the reduction of INTEGRAL data from all four instruments. ISGRI and JEM-X use coded masks to provide imaging information. This means that photons from a source within the field of view (FOV) are distributed over the detector area in a pattern determined by the position of the source in the FOV. Source positions and intensities are determined by matching the observed distribution of counts with those produced by the mask modulation. After the standard data pipeline processing (dead time correction, good time-interval selection, gain correction, and energy reconstruction), source spectra and background subtracted light curves were derived using standard tools in OSA 5.1. The positions of all the detected sources were fixed at the values given in the ISDC Reference Catalogue (version 23.0) which contains all known high-energy sources (see Ebisawa et al. 2003) in order to derive reliable source fluxes. In addition, all sources that are at and above 6 sigma detection limit were extracted simultaneously during the analysis to avoid incorrect photon attribution between sources in order to map the field correctly. The coverage is less for JEM-X due to its smaller FOV compared to ISGRI. For further data manipulation we used standard software tools such as FTOOLS 6.0.4-6.1.1 and XSPEC 12.2.1-12.3.0. Preliminary analysis of light curves and spectra can be found in Balman et al. (2007); Balman (2008).

3. Results

3.1. Light Curves

ISGRI and JEM-X light curves for all the four sources were derived using the standard OSA 5.1 extraction algorithms. Event times were corrected to the solar system barycenter when necessary. The data were grouped in bins of 10 s (XB 1916–053), 180 s (XB 1323–619), 120 s (X 1624–490) and 10 s (4U 1746–371) for the JEM-X analysis. The grouping time was increased to 240 s (XB 1916–053), 240 s (XB 1323–619), 240 s (X 1624–490) and 300 s (4U 1746–371) for the ISGRI analysis in order to increase the signal-to-noise ratio of the light curves. A search was made for any bursting activity since XB 1323–619, 4U 1746–371 and XB 1916–053 are known X-ray burst sources. For XB 1916–053, we detected 14 X-ray bursts with JEM-X, one of which is double

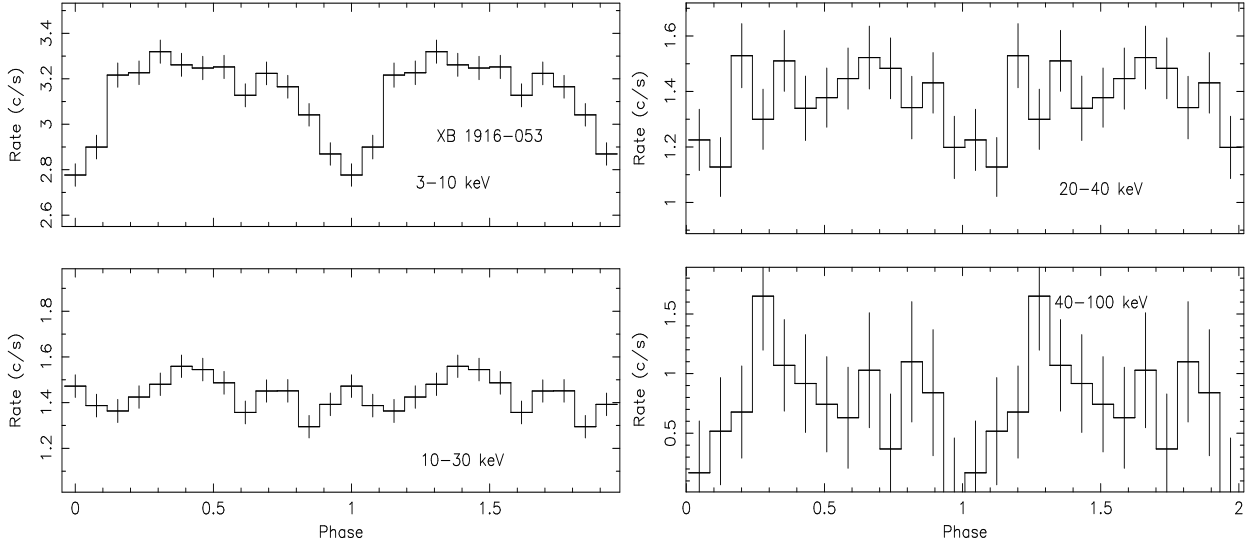


Fig. 1.— JEM-X (3-30 keV) and ISGRI (20-100 keV) folded light curves of XB 1916–053. The energy ranges are indicated on the panels. The folding period is given in Table 1.

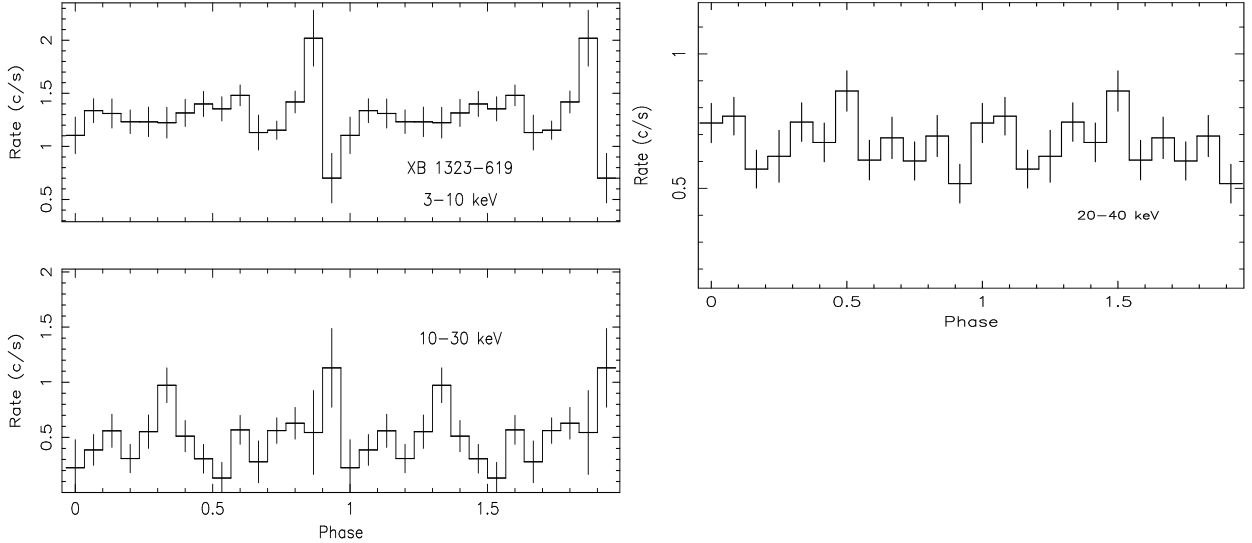


Fig. 2.— JEM-X (3-30 keV) and ISGRI (20-40 keV) folded light curves of XB 1323–619. The energy ranges are indicated on the panels. The folded light curve in the 40–100 keV energy range is not shown because of the low statistical quality. The folding period is given in Table 1.

peaked. For XB 1323–619 some bursts with very low statistical quality were detected and removed from the data. No bursts were detected from 4U 1746–371 or X 1624–490 in either the JEM-X or ISGRI data. Some high intensity data points that appeared in X 1624–490 during non-dipping intervals have been removed while constructing spectra. These are most likely a result of few flaring activities of the source. For XB 1916–053 and X 1624–490 which have well determined dip periods,

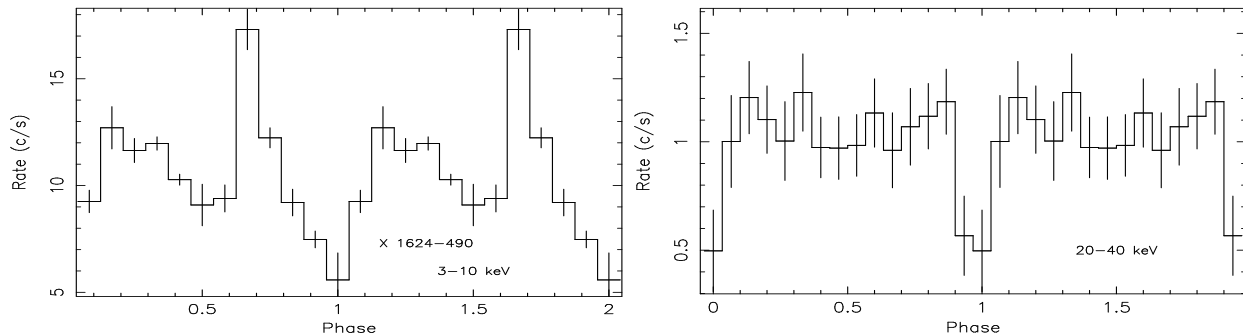


Fig. 3.— JEM-X (3-10 keV) and ISGRI (20-40 keV) folded light curves of X 1624–490. The energy ranges are indicated on the panels. The folded light curve in the 40–100 keV energy range is not shown because of the low statistical quality. The folding period is given in Table 1.

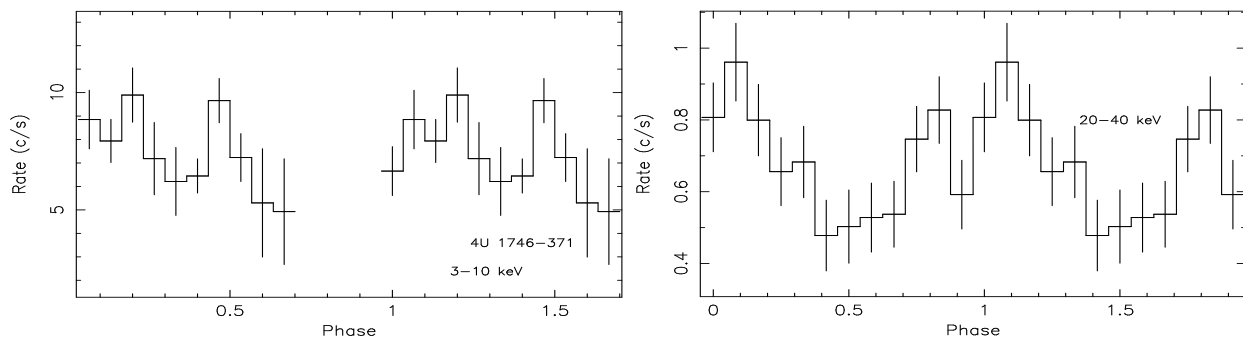


Fig. 4.— JEM-X (3-10 keV) and ISGRI (20-40 keV) folded light curves of 4U 1746–371. The energy ranges are indicated on the panels. Some of the phases that are not covered well or show low statistical quality have been disregarded from the folded light curves. The folded light curves in the 10–30 keV and 40–100 keV energy ranges are not shown because of their low statistical quality. The folding period is given in Table 1.

the uncertainties on the dip occurrence times over the observation duration are small compared with their orbital periods so the light curves from these sources were folded on the dip periods given in Table 1. For XB 1323–619 and 4U 1746–371 the dip periods are not well determined, but the error that should be quadratically added from binning of the light curves to have enough signal to noise does not allow any period error determination better than presently known. We, therefore, also used the periods given in Table 1 for folding. In addition, the phases of the two light curves are arbitrary since we can not lock our epoch with the previous ephemerides due to the error in the periods for these two sources.

Overall, we find dipping/modulation of light curves in all sources (not necessarily in all energy bands) folded on the periods in Table 1. The modulation depth normalized to the mean count rate can be defined as $\% \text{ modulation depth} \sim 100 \times (\text{max rate} - \text{min rate}) / (\text{max rate} + \text{min rate}) / 2$. XB 1916–053 indicate a modulation of 18% in the 3–10 keV energy range. Above 10 keV the JEM-X observations do not show evidence for any dipping activity for the source (see Fig. 1). With

ISGRI, the 20–40 keV reveals about 25% modulation depth. XB 1916–053 reveals only a small modulation of the light curve $< 15\%$ at the orbital period in the 40–100 keV energy range (see Fig. 1). For XB 1323–619, the JEM-X data show modulation of 40% in the 3–10 keV energy range for a small range of phases. It shows no modulation in the higher energies with JEM-X. The ISGRI, 20–40 keV, data show no variation on the X-ray dip period, as well (see Fig. 2). We note that this could be both because of a physical effect (e.g., precession of the disk) or due to large error in period determination. X 1624–490 shows dipping/modulation in the JEM-X light curve of about 25% (see Fig. 3). The ISGRI light curve of the source has a modulation of about 40%. We detect some orbital modulation from 4U 1746–371 in the 3–10 keV (JEM-X) which is less than 10%. The ISGRI light curve shows dipping with about 45% modulation depth (see Fig. 4). A summary of modulation depths at certain energies for each source can be found in Table 3.

We performed Fourier analysis of the time series obtained from the JEM-X and ISGRI data in order to recover the known frequency of orbital modulations, search for new periodic signals, and detect any red-noise features in the low frequency band for XB 1916–053, X 1624–490, and 4U 1746–371. The Scargle Algorithm (Scargle 1982; Press et al. 1992) has been applied in the 3–10 keV range to analyze the JEM-X time series data. Top panels of Figure 5 show Scargle periodograms (no power spectra are averaged). The X-ray dip periods are noted on each panel of the figure (The periods are listed on Table 1. The high peaks in these panels other than the noted periods are false features of high noise. The detection limit of a period at the 3σ confidence level (99%) is at a power level of 16.8 for X 1624–490 and 15.3 for XB 1916–053 and 4U 1746–371 (Scargle 1982). Therefore, the signals (at the dip periods) are at 3σ level for XB 1916–053 and X 1624–490, but the signal is insignificant for 4U 1746–371 and thus, the Scargle periodogram has been omitted. We note that the length of the time series used for both X 1624–490 and XB 1916–053 does not yield better errors than the published ones, thus we avoid comparison of any derived periodicity with the previous detections. However, Figure 5 confirms our folded light curves. In order to correct for the effects of windowing and sampling functions on power spectra, synthetic constant light curves were created and the actual power spectra were checked against the synthetic power spectra for false features. In addition, we did not perform prewhitening or detrending of the light curves.

We also performed power spectral analysis of the 20–40 keV ISGRI light curves in a similar way to the JEM-X lightcurves using Scargle algorithm. However, the periodograms yielded no significant peaks in the power spectra of the three sources. In order to find the origin of the modulations detected in the ISGRI light curves we calculated stacked and averaged power spectra using standard Leahy normalization (Leahy et al. 1983). We have averaged 108, 199, and 11 power spectra for XB 1916–053, X 1624–490 and 4U 1746–371 with 2048, 1024, and 16384 frequency bins in each PSD, respectively. We detect a wide red-noise hump around/in the location of the orbital/dip frequencies in these sources over 3σ (99% Confidence level) detection level and particularly a read noise peak at the location of the X-ray dip period of 4U 1746–371 (see Fig. 5 lower/bottom panel). We do not detect a particular flattening of the red-noise in the 20–40 keV energy band in the frequency range of the orbital/dip periods which should be expected from disk

fed systems (Belloni et al. 2002). We think that the modulations detected above the 20 keV range in Figs.1–4 are affected from these red noise humps, but the peak in 4U 1746–371 is clear and it shows the highest percent modulation in the 20–40 keV range.

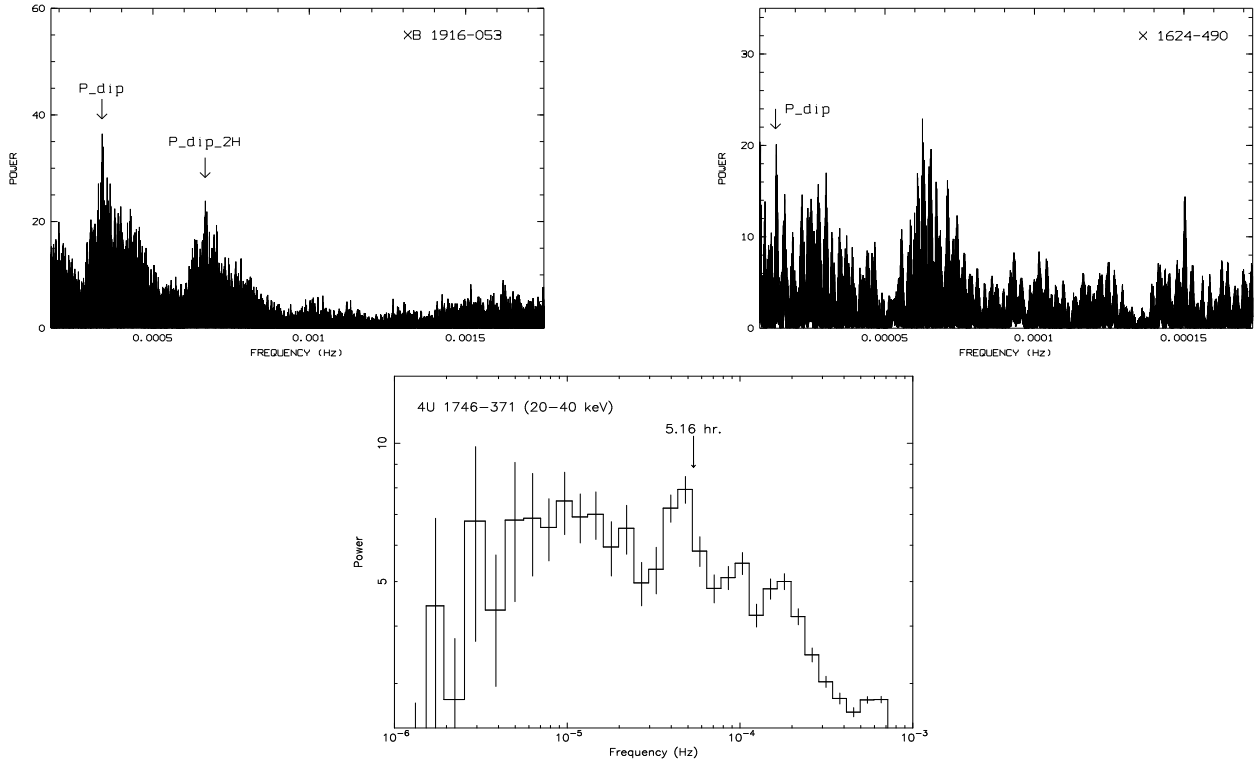


Fig. 5.— Top panels show the power spectra of XB 1916–053 and X 1624–490 between 3–10 keV derived using the Scargle algorithm (i.e., Scargle Periodograms). Source names are given on each panel. The X-ray dip periods are labeled on the panels and 2H refers to the second harmonic of the period. See text for 3σ detection limits for XB 1916–053 and X 1624–490. Bottom panel is the average 20–40 keV power spectra of 4U 1746–371. The expected (white) noise level is subtracted and the lowest level on the y axis corresponds to the 3σ detection limit for 4U 1746–371.

3.2. Spectra

The JEM-X and ISGRI data presented in Table 2 were used to derive a time-averaged broadband spectrum of each of the four LMXBs studied in this paper. This data set provides a unique test that could only be performed with INTEGRAL since it is the only high-energy mission that frequently observes the galactic bulge region with large field of view instruments. During the time span of our observations, we do not detect any prominent high- or low-states of any of the LMXBs in our sample.

We first performed spectral analysis on combined JEM-X and ISGRI spectra using XSPEC version 12.2.1 and 12.3.0 (Arnaud 1996). A constant factor was included in the spectral fitting to allow for a normalization uncertainty between the two instruments. This factor was constrained to be within the expected range (i.e., 0.6–0.7) as (see Kirsch et al. (2005)) as the parameter was thawed during the fitting procedure. Spectral uncertainties are given at 90% confidence level ($\Delta\chi^2=2.71$ for a single parameter) and upper limits at 95% confidence. We regrouped the JEM-X energy channels (1–256) by a factor of 3–4 to increase the signal-to-noise in the spectra. We used linearly sampled 40 channel response matrices for the ISGRI data where the data were similarly regrouped by a factor of 4–6. After the regrouping process, energy channels that have low signal-to-noise ratio have also been ignored. To account for systematic effects we added quadratically a 1% uncertainty to each spectral bin as recommended in the OSA 5.1 cookbook. We note that the addition of 1-2% uncertainty for statistical concerns only *reduces* the χ^2_ν values, but does not affect the best fit parameters or parameter ranges.

We fitted composite models to the broad-band spectra consisting of a disk blackbody (Mitsuda et al. 1984; Makishima et al. 1986; Mitsuda et al. 1989) or a blackbody, together with either a cutoff power-law or `CompTT` model (Titarchuk 1994; Hua & Titarchuk 1995). Table 4 shows the best-fit spectral parameters and their uncertainty ranges at 90% confidence level for each composite model. The disk blackbody or blackbody model was used to account for the emission from the disk and/or neutron star. The emission from an extended scattering/Comptonizing region was accounted for by the XSPEC model `CompTT`, a more physical model compared with the generic cut-off power-law model that only involves a simple power law decay with a high energy cut-off depending on the energy of the scattering electrons. During the fitting procedure, we also included the `wabs` XSPEC model to account for the neutral hydrogen absorption. These values were fixed at the values derived from the XMM-Newton data (Boirin et al. 2005; Díaz Trigo et al. 2006) (also compared with the N_H values derived from the Beppo-SAX and R-XTE data to make sure all of them are similar). Figure 6 displays the fitted broad-band spectra of the four LMXBs.

We also applied a single model to fit the four broad-band spectra. We used four models; the cut-off power law, `CompTT`, blackbody, or the disk blackbody for the analysis and found that none of the four LMXB spectra are consistent with a single emission model yielding reduced χ^2 values >2.5 and/or nonphysical parameters except for XB 1323–619. A fit of a power-law model with absorption to the spectra of XB 1323–619 yields an N_H of $5.5^{+3.0}_{-2.9} \times 10^{22} \text{ cm}^{-2}$ with a power law photon index of $2.9^{+0.08}_{-0.09}$ and a normalisation of $0.6^{+0.15}_{-0.2} \text{ photons keV}^{-1} \text{ cm}^{-2} \text{ s}^{-1}$ at 1 keV ($\chi^2_\nu = 1.5$). We also fitted the 4-200 keV spectra with a double blackbody or double disk-blackbody model. The fits resulted in reduced χ^2 values >2.0 and/or nonphysical parameters for all sources.

The X-ray spectrum of X 1624–490 and XB 1323–619 as been modeled using a halo model because of the extensive dust in the vicinity of the sources particularly of X 1624–490 (Xiang et al. 2007; Smale et al. 2001; Díaz Trigo et al. 2006; Bałucińska-Church et al. 2000; Barnard et al. 2001). The radial intensity profiles of a source is expected to have excess over the point spread function due to the level of dust scattering at low energies mainly below 5-6 keV. We also applied the *dust*

model in XSPEC to the INTEGRAL spectra along with the two-component model of emission. This multiplicative model modifies a spectrum due to scattering off dust on the line-of-sight. The model assumes that the scattered flux goes into a uniform disk whose size has a $1/E$ dependence and whose total flux has a $1/E^2$ dependence. The spectral results in Table 4 do not change with the inclusion of the multiplicative model. This is expected given the sensitivity, the large scale of the point spread function of INTEGRAL detectors and the energy range we are applying the model which is above 4 keV. We note that the detected blackbody temperatures (for the the two sources) are the same as the Beppo-Sax results including the dust contribution which means that the INTEGRAL spectra is not affected by dust scattering component.

We also divided the JEM-X and ISGRI data into dipping and non-dipping episodes by selecting on phase intervals and created spectra for the LMXBs in our sample. The dip-phase bins in Figs. 1–3 (phases 0.9–1.05) were used together with the periods in Table 1. The extracted dips are an average over different levels of dipping, but the phase bins approximates the levels closest to the deepest dips Díaz Trigo et al. (2006); Barnard et al. (2001). We were able to recover statistically significant and different dip and non-dip spectra for XB 1916–053 and X 1624–490. The analysis of the 4U 1746–371 data did not reveal any difference in the dip and non-dip spectra. Given the low count rates and the short dip intervals observed from XB 1323–619, we could not derive a statistically significant dip spectra with JEM-X in 15 ksec (dipping time in the given exposure time) and the high energies (ISGRI) show no variation, hence no dipping activity at the given period (see Fig. 2).

Fig. 7 shows the simultaneously fit dip and non-dip spectra of XB 1916–053 and X 1624–490 with only a composite model of a blackbody and `compTT`. The top right hand panel of Fig. 7 shows the fitted XB 1916–053 spectra and the top left panel shows the X 1624–490 spectra. The composite spectral model was simultaneously fit to the dip and non-dip spectra of the two sources for a better determination of the differences in the fitted results (the fitted model was `wabs*(bbody+compTT)`). The residuals of the top panels of Fig. 7 indicate distinctive deviations from the mean and the reduced χ^2 values are >2.4 in the top panels (the d.o.f. are similar to the ones reported on Table 4). Acceptable fits were achieved when two different neutral hydrogen column densities for dip and non-dip spectra were assumed along with an additional absorption line at 6.9 keV for XB 1916–053 (dip spectra) and an emission line for X 1624–490 (non-dip spectra) in the fitting process (additional models of `gabs` and `gauss` were used for modeling the lines). The spectral parameters for the composite blackbody and `compTT` model of the dip and non-dip spectra for XB 1916–053 and X 1624–490 resemble the best fit values on Table 4 very closely, so we do not include them in this paragraph. On the other hand, we found a previously detected (Boirin et al. 2004) absorption line in XB 1916–053 at $6.9_{-1.8}^{+0.6}$ keV. Addition of the line improves the fluctuation of the (fit) residulas from above 2σ down to less values in the vicinity of 6-7 keV. We also found a previously detected emission line in the non-dip spectrum of X 1624–490 at $6.8_{-0.2}^{+0.2}$ keV with an integrated flux of $2.1_{-0.8}^{+0.9} \times 10^{-3}$ photons $\text{s}^{-1} \text{cm}^{-2}$. Addition of the line improves the fluctuation of the (fit) residulas from 3σ down to less values in the vicinity of 6-7 keV.

The detection of an increased amount of absorption in dip spectra for both sources together with the presence of an absorption line in XB 1916–053 suggests the existence of photoionized absorbers solely from the INTEGRAL data. However, INTEGRAL data, alone, does not account for existence of photoionized absorbers in the persistent emission. Fig. 7 middle and bottom panels show the non-dip and dip spectral fits to both XB 1916–053 and X 1624–490. In order to compare with the results from the XMM-Newton analysis of these two sources with models of photoionized absorbers, we applied the warm absorber model, **warmabs** (an additional model in XSPEC), compiled with XSPEC 12.3.0 to both spectra of XB 1916–053 and X 1624–490. **Warmabs** models the absorption from a photoionized plasma in the line of sight. Column densities of ions (including small cross-sections) are coupled through a photoionization model. **Warmabs** calculates spectra using stored level populations calculated by XSTAR (Kallman & Bautista 2001; Bautista & Kallman 2001, 2000) assuming a given continuum spectrum. For the ionizing flux a photon index of $\Gamma = 2$ was assumed in this study consistent with the X-ray observations of these systems. The spectral parameters of **warmabs** are an absorption column density of hydrogen of the photoionized plasma, the logarithm of the ionization parameter $\log(\xi)$, and the turbulent velocity broadening σ_v along with elemental abundances. The ionization parameter $\xi = L/nR^2$ where L is the luminosity of the ionizing source, n is the gas density, and R is the distance from the ionizing source. The middle panels in Fig. 7 show the non-dip and the bottom panels show the dip spectra fitted with the composite model of a neutral hydrogen absorption, a blackbody and a **compTT** including a **warmabs** model to account for the excessive absorption and/or the absorption line. The fits performed with the dip and non-dip spectra of XB 1916–053 and X 1624–490 yield reduced χ^2 values around 1.0–0.83 (for 36–31 d.o.f.) . Using the fits to the INTEGRAL data, we derive a $\log(\xi)$ of $3.8_{-0.4}^{+0.2}$ for the persistent and $2.8_{-0.2}^{+0.2}$ for the dip spectra of XB 1916–053. The absorption column of the ionized absorber is $4.8_{-1.3}^{+1.3} \times 10^{22} \text{ cm}^{-2}$ during the dipping episodes and $1.7_{-1.5}^{+1.5} \times 10^{22} \text{ cm}^{-2}$ during non-dipping intervals. The fits performed with the dip and non-dip spectra of X 1624–490 yield a $\log(\xi)$ of $3.4_{-0.2}^{+0.2}$ for the persistent and $2.6_{-0.2}^{+0.2}$ for the dip spectra. The fit results indicate an absorption column of $4.0_{-1.9}^{+1.9} \times 10^{22} \text{ cm}^{-2}$ for the ionized absorber in the persistent and $15.8_{-1.6}^{+1.6} \times 10^{22} \text{ cm}^{-2}$ in the dipping spectra. The N_H parameter to the line of sight are kept constant as in Table 4 during analysis. The parameter σ_v was fixed at the values determined from XMM-Newton observations (Díaz Trigo et al. 2006); fixed at the values of 100 km s⁻¹ (dip) and 300 km s⁻¹ (non-dip) for X 1624–490 and 200 km s⁻¹ (dip) and 2000 km s⁻¹ (non-dip) for XB 1916–053.

4. Discussion

We report the results of archival INTEGRAL observations of four dipping LMXBs, XB 1916–053, XB 1323–619, 4U 1746–371 and X 1624–490. The data presented in Table 2 were used to derive time-averaged broad-band spectra of the four LMXBs (January 2003–November 2004) which is a unique capability of the INTEGRAL observatory as the data analysis is performed by averaging observation science windows over long periods of time. We, also, investigated the dip and non-dip spectra. During the time span of our data, we do not detect a prominent high or low state of any

of the LMXBs in our sample.

The LMXB spectra have been assumed using several different approaches. One of the approaches, Western model (White et al. 1988), is a two-component emission model where the harder X-ray component is the Comptonized emission originating from an ADC in the LMXB spectra and it has the form of a power-law with an energy cut-off at the limit of the Comptonizing electrons and only the very bright sources required an additional blackbody component from the boundary layer between the accretion disk and the surface of the neutron star. Another model, Eastern model (Mitsuda et al. 1989), assumes that photons from the neutron star are Comptonized in a small central region on the disk and harder component originates from a multi-temperature disk blackbody model. A descendent model, Birmingham model (Church & Balucinska-Church 1995), takes after the Western model, but assumes neutron star blackbody for the soft components. High-resolution spectroscopic observations of LMXBs have shown in some cases the presence of extended X-ray emitting plasmas or outflows surrounding the accretion disk. The detection of these components and their kinematic properties has been made possible by the observation of emission or absorption lines from very highly ionized metals. This also diagnoses several different emitting zones in LMXBs such as disk atmospheres and coronae (Jimenez-Garate et al. 2002, 2003). In this paper, we fitted spectra assuming several different models and constructed Table 4 to test the INTEGRAL data given the presumed approaches to derive the spectral parameters, also, introducing a warm absorber model to model the absorption over 4–200 keV in the light of recent model construction for dipping LMXBs.

This INTEGRAL study uses better S/N spectra and lightcurves incomparison with other studies, particularly above 20 keV for the four LMXBs in question. None of the RXTE studies of these four sources include usable spectra or light curve above 20 keV. The Beppo-Sax has the opportunity to extend out to 100 keV using the PDS instrument which has been used in the literature. However, the shorter exposures 15-30 ksec and low count rates, do not allow for a high S/N spectra above 20 keV, the effective area also falls readily and there are no PDS light curves available in the literature above 20 keV. In general, for two of the sources 4U 1746–371 and X 1624–490, there is no effective study of the spectra or light curve above 15-20 keV. For XB 1916–053 and XB 1323–619 the PDS spectra have been helpful, however the S/N is not favorable to the INTEGRAL study here. INTEGRAL countrates are three to four times better for above 500 ksec integration time (we used about 1 Msec exposure on each source with ISGRI). As a result ISGRI results in this study provide new information on these objects and they are supported by the JEM-X detector (to avoid cross-calibration issues that could arise from using other observatory data) to provide large energy band coverage.

Our spectral results in Table 4 yield blackbody temperatures of 1.7 keV and 1.4 keV, for XB 1323–619 and X 1624–490 which are in excellent agreement with the BeppoSax results (see 1) within statistical errors. On the other hand, XB 1916–053 and 4U 1746–371 yields different blackbody temperatures of 2.3 keV and 0.6 keV, respectively where the BeppoSax results reveal 1.62 keV and 0.5 keV for the same sources (see 1). The INTEGRAL result and BeppoSax results

for 4U 1746–371 agree within statistical errors. Moreover, the Wien photon temperature kT_0 (parameter–seed in photons) varies in a range 0.4–2.5 keV in the four sources (even if we derive similar blackbody temperatures). These differences could be attributed to the existence of more than one blackbody component for at least the cases like XB 1916–053 and 4U 1746–371. At sufficiently high mass accretion rates, the boundary layer and the accretion disk are both radiating in the optically thick regime with kT 1–2 keV. It is expected on theoretical grounds and demonstrated that the boundary layer has higher temperature than the accretion disk yielding two different blackbody temperatures in the X-ray spectra (Gilfanov et al. 2003; Göğüş et al. 2007).

We find that the normalisation parameter for the disk blackbody model, proportional to $R_{in}^2 \cos\theta$, yields fairly small real inner disk radii of less than 14.5 km, 5.2 km, and 12.8 km (all at 3σ maximum limit) for XB 1323–619, XB 1916–053, and X 1624–490, respectively (θ is the inclination angle suitably taken between 60° – 80°). We stress that at 2σ limit these radii are less than a neutron star size. On the other hand, this value is between 27–37 km for 4U 1746–371. As a result, a disk blackbody emission is very unlikely for the three sources except for 4U 1746–371. We note that the 3σ maximum limits on apparent inner disk radii are corrected to real radii according to Kubota et al. (1998). We caution that normalisation of the disk blackbody model involve distance in the calculation which results in a slight uncertainty. Radii change only linearly with distance and only a factor of 2–3 times (in kpc) difference in distance will effect the general trend discussed above. In comparison with this, we derived the size in radii of the blackbody emitting regions for the four sources. We calculate that for XB 1323–619 and XB 1916–053 the radii is between 0.8–1.02 km. For X 1624–490, this radius is about 9.7–11.1 km (e.g., the size of a neutron star). 4U 1746–371 shows an emitting region of 37–51 km which is physically inconsistent with emission from the surface of a neutron star. These ranges above correspond to 3σ error ranges of the used parameters. INTEGRAL results suggests that XB 1323–619 and XB 1916–053 accrete to a small region on the surface of the neutron star and 4U 1746–371 shows only a disk blackbody or boundary layer emission. The disk blackbody temperature of 4U 1746–371 detected in this study is consistent with the BeppoSax results as well (see 1) with only slight difference in disk blackbody temperature. It is difficult to make such deductions for X 1624–490 using solely INTEGRAL data except that a disk blackbody emission is inconsistent with the source. In addition, we note that the normalisation of the blackbody model involve distance in the calculation resulting in some uncertainty. Radii change only linearly with distance. As a result, a factor of only 10 times difference in distance for the case of XB 1916–053 and XB 1323–619 and a factor of only 2–3 difference in the case of X 1624–490 will effect the general trend discussed above.

A comparison with the spectral results obtained from the BeppoSax and R-XTE observations using the Cut-off power-law model for the second emission component shows that the time average data yield somewhat different results for the E_{cut} and the photon index parameters (see Table 4 for individual results). For XB 1916–053, Church et al. (1998) find $\Gamma = 1.61 \pm 0.01$ and $E_{cut} = 80 \pm 10$ keV and Narita et al. (2003b) find a range of powerlaw indices between 1.74–2.05 and E_{cut} of > 30 keV (90% confidence limits). Our results are consistent with R-XTE observation analyses.

For X 1624–490, Bałucińska-Church et al. (2000) find $\Gamma = 2.0 \pm 0.06$ and $E_{\text{cut}} > 12$ keV where we find a photon index > 0.84 and a low E_{cut} value of 1.23–4.6 keV including uncertainty ranges. For 4U 1746–371, Parmar et al. (1999) find $\Gamma < 0.5$ and $E_{\text{cut}} = 0.90 \pm 0.26$ keV where we find $\Gamma = 2.18 \pm 0.8$ and E_{cut} value of 6.6–11.2 keV. For XB 1323–619, Bałucińska-Church et al. (1999) find $\Gamma = 1.48 \pm 0.01$ and $E_{\text{cut}} = 44 \pm 5.1$ keV (BeppoSax results) and Barnard et al. (2001) derive $\Gamma = 1.23 \pm 0.07$ and $E_{\text{cut}} > 44$ keV (R-XTE results). Our results yield $\Gamma = 3.0 \pm 0.2$ and an unbound cut-off energy larger than 156 keV. Barnard et al. (2001) results show an $\Gamma = 1.89$ – 1.91 for $E_{\text{cut}} > 117$, however without inclusion of a blackbody model (90% confidence limits). These are discrepancies regardless of error estimates and such differences between the E_{cut} and the photon index parameters exists also between BeppoSax and R-XTE results. Apart from the fact that there are possible cross-calibration inconsistencies, and that the sources could be variable, this could also be attributed to the Cut-off power-law model being an inadequate model of emission to represent the data in the harder energies particularly in the ISGRI energy band (e.g., relativistic effects). This strengthens the fact that the Comptonizing plasmas in these systems needs to be modeled more properly.

We applied the CompTT model in XSPEC in order to account for the Compton scattering regions in these systems and found a range of plasma temperatures of $18.8_{-6.0}^{+10.9}$ keV for XB 1916–053, $196.4_{-18.8}^{+28.5}$ keV for XB 1323–619, $9.2_{-1.9}^{+2.5}$ keV for X 1624–490 and $4.9_{-2.0}^{+5.6}$ keV for 4U 1746–371 given the best fit results of time-averaged data. These temperatures indicate persistent hot Comptonizing regions, accretion disk coronae (ADCs), in these systems. The optical depth of Compton scattering regions can, also, be derived from the fits, τ , is in a range $0.9_{-0.6}^{+0.7}$ for XB 1916–053, $0.006_{-0.004}^{+0.001}$ for XB 1323–619, $0.2_{-0.2}^{+4.2}$ for X 1624–490 and $1.1_{-0.9}^{+2.3}$ for 4U 1746–371 which, in addition, indicates that the Comptonizing regions are relatively tenuous. XB 1323–619 has the lowest value. Using the model parameter descriptions of CompTT, $n_e \simeq \tau^2 / r_{\text{ad}} \sigma_T$ at high optical depth (Titarchuk 1994; Hua & Titarchuk 1995), we derived maximum limits for the electron densities in the X-ray emitting regions of the four systems as: XB 1916–053, $n_e < 7.6 \times 10^{14} \text{ cm}^{-3}$, 4U 1746–371, $n_e < 1.4 \times 10^{15} \text{ cm}^{-3}$, X 1624–490, $n_e < 1.1 \times 10^{15} \text{ cm}^{-3}$, and XB 1323–619, $n_e < 5.4 \times 10^9 \text{ cm}^{-3}$. We have assumed $0.25 \times r_{\text{ad}}$ for the emitting region (r_{ad} taken from Church & Bałucińska-Church 2004). If the emitting region is $0.1 \times r_{\text{ad}}$ the densities increase by a factor of four. If it is spread over the entire disk, the densities are a factor of four less. The electron densities that can be calculated from the ionization parameters derived from the fits with photoionized absorbers for these systems in Díaz Trigo et al. (2006) yield a range of 8 – $0.2 \times 10^{13} \text{ cm}^{-3}$ for the ionized absorbers in these systems. These values are consistent with the maximum limits in the Comptonizing regions. Then, the suggested warm absorbing regions may have similar densities with the existing coronal regions.

The Compton radius in an accretion disk corona (ADC) with temperature kT is $r_C \simeq GM_{\text{p}} / kT_{\text{plasma}}$ (cf., Church & Bałucińska-Church 2004; Bałucińska-Church & Church 2005) where the hydrostatic equilibrium fails. Outside this radius, the corona will dissipate as a wind. Church & Bałucińska-Church (2004) shows that the Compton radii for some LMXB dippers and the ADC radii calculated from the ingress and egress timescales in their lightcurves are very similar. We calculated the Compton radii for the four LMXBs given the plasma temperatures from the fits with the CompTT model as

follows : XB 1916–053 has $r_C \simeq 1.3 \times 10^{10}$ cm, 4U 1746–371 has $r_C \sim 1.8 \times 10^{10}$ cm, X 1624–490 has $r_C \sim 3.9 \times 10^{10}$ cm, and XB 1323–619 has $r_C \sim 1.1 \times 10^9$ cm. The extent of the Comptonizing regions, except for XB 1323–619, are large and it could cover 13-77% of the disk (by area) given the statistical errors on the plasma temperature. For XB 1323–619 the coverage of the ADC is only about 1% of the disk (by area), most likely a small region confined to inner parts of the disk (given the size of calculated r_C).

We have also modeled the absorption in the broad-band INTEGRAL energy range with photoionized absorbers owing to the detection of mainly iron absorption lines from these systems (other absorption lines have also been detected). We were able to satisfactorily separate dip and non-dip spectra from two of the systems and studied, for the first time, 4-200 keV spectra modeling photoionized absorbers in these systems. A comparison of the spectral results with the XMM-Newton analysis in the 0.2-15.0 keV band (see Table 1) yields $\log(\xi)$ values larger in the case of XB 1916–053 and slightly smaller in the case of X 1624–490 for both non-dip spectra obtained from the time-averaged INTEGRAL data. For dip spectra both sources show slightly higher ionization parameter (compared with deepest dips in the XMM-Newton analysis). This shows that INTEGRAL detects a more highly ionized absorber in XB 1916–053 (even higher than X 1624–490) which was not recovered in the 0.2-15.0 keV analysis. The neutral absorption of the highly ionized absorber is significantly lower compared with the XMM-Newton results at all times. The XMM-Newton analysis, also, assumes a photon index of $\Gamma = 2$ for the ionizing spectrum as assumed in this analysis, but with an additional cut-off energy of 86 keV and 12 keV for XB 1916–053 and X 1624–490, respectively. A comparison with the *Chandra* (0.3-10.0 keV) spectral results of the non-dip emission shows that INTEGRAL detects the same $\log(\xi)$ parameter. A value of 3.73 ± 0.13 is derived by Juett & Chakrabarty (2006) assuming a power law of -1 for the incident ionizing flux. For X 1624–490 Iaria et al. (2007) measures approximately a $\log(\xi)$ of 4.1 for the non-dip spectra which is higher than the INTEGRAL result.

5. Summary and Conclusions

We have investigated 4–200 keV broad-band spectrum and temporal characteristics of four dipping LMXB systems, XB 1916–053, XB 1323–619, X 1624–490, and 4U 1746–371. INTEGRAL has shown us for the first time the time-averaged spectral parameters of these systems together with the dip and non-dip spectra. This study also demonstrates for the first time, a high sensitivity study of spectra and timing characteristics of these four LMXBs above 20 keV (simultaneously with 3-20 keV band data). INTEGRAL reveals the spectral characteristics of the hottest regions in these dipping LMXBs together with the nature of the absorbers within the systems. We find that the persistent emission spectral parameters of X 1624–490 and XB 1916–053 remain mostly the same in and out the dipping intervals given the 4-200 keV energy range except for the changing absorption below 10 keV for the two systems. 4U 1746–371 shows a spectrum that is consistently the same, in and out the X-ray dips between 4–200 keV given the INTEGRAL sensitivity. INTEGRAL spectra

are consistent with existence of persistent hot Comptonizing coronal regions (ADCs), with plasma temperatures using Comptonized plasma models as $18.8_{-6.0}^{+10.9}$ keV for XB 1916–053, $196.4_{-18.8}^{+28.5}$ keV for XB 1323–619, $9.2_{-1.9}^{+2.5}$ keV for X 1624–490 and $4.9_{-1.9}^{+5.6}$ keV for 4U 1746–371. We caution that the ADC temperature for XB 1323–619 is very high in comparison to the rest and even within the LMXBs and the temperature limit of the CompTT model to satisfactorily represent the ADC falls readily after 50 keV (Farinelli et al. 2008). Using our fits, we derive a range of optical depth to Compton scattering τ in these regions as $0.9_{-0.6}^{+0.7}$ for XB 1916–053, $0.006_{-0.004}^{+0.001}$ for XB 1323–619, $0.22_{-0.20}^{+4.21}$ for X 1624–490 and $1.1_{-0.9}^{+2.3}$ for 4U 1746–371. Given these results XB 1323–619 has, by a large factor, the hottest ADC with the lowest optical depth. None of the sources exhibit spectra consistent with a single model of emission except for XB 1323–619 (i.e., a single power law model can be used to model the spectra). Therefore, we stress that the spectra of these sources should never be fitted using a single model of emission regardless of the energy band (i.e., as in *Chandra* or XMM-Newton bands). In addition, the four systems can not be fitted, alone, with a double blackbody emission or double disk-blackbody emission models, either. Fits to the INTEGRAL spectra suggests a third component particularly of blackbody nature (due to the detected different seed-in photon temperature compared with blackbody temperature) that could be existent in the spectra.

For the first time, we detect $\sim 15\%$, 40% , and 45% modulation depth (variation normalized to mean flux) in the 20–40 keV energy range at the X-ray dip periods from XB 1916–053, X 1624–490, and 4U 1746–371, respectively. We believe this could be as a result of scattering off of the bulge at the accretion impact zone (fixed in the orbital plane). Photoelectric absorption by material at the impact zone is not as desirable an explanation since after 20 keV Comptonization and energy independent scattering is expected to dominate. This is also supported by the large red noise (humps) found in the average power spectra above 20 keV.

We have studied the effects of photoionized absorbers in dipping LMXBs for the first time in a broad energy band 4–200 keV from XB 1916–053 and X 1624–490. We find that the most highly ionized absorber is in XB 1916–053 with an ionization parameter $\log(\xi)$ of $3.8_{-0.4}^{+0.2}$ although X 1624–490 has more luminosity. This indicates the importance of system geometry and size. Moreover, inclusion of spectra from a harder energy band compared with the XMM-Newton or Chandra data help to constrain the absorber properties better.

The INTEGRAL spectrum reveals a small size accretion region that is less than 1 % of the surface area of a typical neutron star in an LMXB derived from the blackbody fits for XB 1916–053 and XB 1323–619. This is difficult to explain, alone, by the large amount of scattering in these systems. On the contrary, accretion region sizes either about the size of a neutron star or 16–20 times larger (than a neutron star in terms of accretion surface area) are consistent with X 1624–490 and 4U 1746–371, respectively. Such results from INTEGRAL reveals different accretion geometries and emission regions for these dipping LMXB systems in contrast with the very similar modeling of such regions used in previous studies (i.e., XMM-Newton, RXTE, Beppo-Sax).

The INTEGRAL broad-band hard X-ray and γ -ray emission from the four dipping LMXB systems show that these systems have different Comptonizing regions in size and in plasma temperature and has different accretion geometries and emitting regions. We calculate that Comptonizing coronal regions cover a larger fraction of the disk and are colder in comparison with the conventional ADCs in three systems (i.e., XB 1916–053, X 1624–490, 4U 1746–371), such regions vary with respect to the source and are not only strongly dependent on the central source luminosity. INTEGRAL detects that ADC in XB 1323–619 is much smaller in size (much more hotter) in comparison to the other three systems and probably confined to the inner regions of the disk. We do not find a direct correlation of source luminosity with plasma temperature in the ADCs of the four systems. These extended highly ionized coronal regions (ADCs) may act as an absorber to the incident radiation (Church et al. 2005). As a result, we would be viewing these systems through highly ionized absorbing regions at all times. On the other hand, INTEGRAL results confirms the existence of warm absorbing regions and that the absorbing material looks less photoionized during the main dips and more ionized as viewed in the persistent emission intervals in a broad energy band of 4–200 keV for at least two of the dippers XB 1916–053 and X 1624–490. These absorbing regions can be associated with an accretion disk atmosphere (e.g., EXO 0748–676: Jimenez-Garate et al. 2003) However, the two systems are not well known X-ray line emitters. It is unclear, at this stage, if the absorber is the same in a given location, or if different absorbers are viewed during dipping and persistent emission episodes. It may be that it is a combined effect of different absorbing regions throughout the disk (e.g., inner disk and outer disk) superimposed on the spectra.

SB would like to thank Arvind Parmar, for introducing the topic of dipping LMXBs and warm absorbers, and helpful discussions in constructing the paper. I would also like to thank Mariano Mendez, Tim Oosterbroek, Maria Diaz Trigo, Ada Paizis, Lara Sidoli for discussions, help with data analysis and critical reading of the manuscript. This research was based on observations with INTEGRAL, an ESA project with instruments and science data centre funded by ESA member states (especially the PI countries: Denmark, France, Germany, Italy, Switzerland, Spain), Czech Republic and Poland and with the participation of Russia and the USA. SB acknowledges an ESA fellowship. SB also acknowledges support from TÜBİTAK, The Scientific and Technological Research Council of Turkey, through project 106T040.

REFERENCES

- Arnaud, K. A. 1996, in ASP Conf. Ser. 101: Astronomical Data Analysis Software and Systems V, 17
- Balman, Ş. 2008, in American Institute of Physics Conference Series, Vol. 983, 40 Years of Pulsars: Millisecond Pulsars, Magnetars and More, ed. C. Bassa, Z. Wang, A. Cumming, & V. M. Kaspi, 530–532

- Balman, S., Parmar, A. N., Sidoli, L., & et al. 2007, in ESA Special Publication, Vol. 622, ESA Special Publication, 417–420
- Bałucińska-Church, M., Church, M. J., & Smale, A. P. 2004, MNRAS, 347, 334
- Bałucińska-Church, M., Humphrey, P. J., Church, M. J., & Parmar, A. N. 2000, A&A, 360, 583
- Bałucińska-Church, M., & Church, M. J. 2005, in American Institute of Physics Conference Series, Vol. 797, Interacting Binaries: Accretion, Evolution, and Outcomes, ed. L. Burderi, L. A. Antonelli, F. D’Antona, T. di Salvo, G. L. Israel, L. Piersanti, A. Tornambè, & O. Straniero, 339–344
- Bałucińska-Church, M., Church, M. J., Oosterbroek, T., Segreto, A., Morley, R., & Parmar, A. N. 1999, A&A, 349, 495
- Barnard, R., Bałucińska-Church, M., Smale, A. P., & Church, M. J. 2001, A&A, 380, 494
- Bautista, M. A., & Kallman, T. R. 2000, ApJ, 544, 581
- . 2001, ApJS, 134, 139
- Belloni, T., Psaltis, D., & van der Klis, M. 2002, ApJ, 572, 392
- Boirin, L., Barret, D., Olive, J. F., Bloser, P. F., & Grindlay, J. E. 2000, A&A, 361, 121
- Boirin, L., Méndez, M. Díaz Trigo, M., Parmar, A. N., & Kaastra, J. 2005, A&A, 436, 195
- Boirin, L., Parmar, A. N., Barret, D., Paltani, S., & Grindlay, J. E. 2004, A&A, 418, 1061
- Callanan, P. J., Grindlay, J. E., & Cool, A. M. 1995, PASJ, 47, 153
- Chou, Y., Grindlay, J. E., & Bloser, P. F. 2001, ApJ, 549, 1135
- Church, M. J., & Bałucińska-Church, M. 1995, A&A, 300, 441
- Church, M. J., & Bałucińska-Church, M. 2004, MNRAS, 348, 955
- Church, M. J., Dotani, T., Bałucińska-Church, M., Mitsuda, K., Takahashi, T., Inoue, H., & Yoshida, K. 1997, ApJ, 491, 388
- Church, M. J., Parmar, A. N., Bałucińska-Church, M., Oosterbroek, T., Dal Fiume, D., & Orlandini, M. 1998, A&A, 338, 556
- Church, M. J., Reed, D., Dotani, T., Bałucińska-Church, M., & Smale, A. P. 2005, MNRAS, 359, 1336
- Cottam, J., Kahn, S. M., Brinkman, A. C., den Herder, J. W., & Erd, C. 2001, A&A, 365, L277
- Courvoisier, T. J. L., Parmar, A. N., Peacock, A., & Pakull, M. 1986, ApJ, 309, 265

- Courvoisier, T. J.-L., Walter, R., Beckmann, V., Dean, A. J., Dubath, P., Hudec, R., Kretschmar, P., Mereghetti, S., Montmerle, T., Mowlavi, N., Paltani, S., Preite Martinez, A., Produit, N., Staubert, R., Strong, A. W., Swings, J.-P., Westergaard, N. J., White, N., Winkler, C., & Zdziarski, A. A. 2003, *A&A*, 411, L53
- Díaz Trigo, M., Parmar, A. N., Boirin, L., Mendez, M., & Kaastra, J. 2006, *A&A*, 445, 179
- Díaz Trigo, M., Parmar, A. N., Boirin, L., Motch, C., Talavera, A., & Balman, S. 2009, *A&A*, 493, 145
- Ebisawa, K., Bourban, G., Bodaghee, A., Mowlavi, N., & Courvoisier, T. J.-L. 2003, *A&A*, 411, L59
- Farinelli, R., Titarchuk, L., Paizis, A., & Frontera, F. 2008, *ApJ*, 680, 602
- Forman, W., Jones, C., Cominsky, L., Julien, P., Murray, S., Peters, G., Tananbaum, H., & Giacconi, R. 1978, *ApJS*, 38, 357
- Frank, J., King, A. R., & Lasota, J. P. 1987, *A&A*, 178, 137
- Galloway, D. K., Chakrabarty, D., Munro, M. P., & Savov, P. 2001, *ApJ*, 549, L85
- Gilfanov, M., Revnivtsev, M., & Molkov, S. 2003, *A&A*, 410, 217
- Göğüş, E., Alpar, M. A., & Gilfanov, M. 2007, *ApJ*, 659, 580
- Hua, X.-M., & Titarchuk, L. 1995, *ApJ*, 449, 188
- Iaria, R., Di Salvo, T., Lavagetto, G., Robba, N. R., & Burderi, L. 2006, *ApJ*, 647, 1341
- Iaria, R., Lavagetto, G., D’Aí, A., di Salvo, T., & Robba, N. R. 2007, *A&A*, 463, 289
- Jimenez-Garate, M. A., Raymond, J. C., & Liedahl, D. A. 2002, *ApJ*, 581, 1297
- Jimenez-Garate, M. A., Schulz, N. S., & Marshall, H. L. 2003, *ApJ*, 590, 432
- Jones, M. H., & Watson, M. G. 1989, in *ESA SP-296: Two Topics in X-Ray Astronomy, Volume 1: X Ray Binaries. Volume 2: AGN and the X Ray Background*, ed. J. Hunt & B. Battick, 439–444
- Jonker, P. G., van der Klis, M., & Wijnands, R. 1999, *ApJ*, 511, L41
- Juett, A. M., & Chakrabarty, D. 2006, *ApJ*, 646, 493
- Kallman, T., & Bautista, M. 2001, *ApJS*, 133, 221

- Kirsch, M. G., Briel, U. G., Burrows, D., Campana, S., Cusumano, G., Ebisawa, K., Freyberg, M. J., Guainazzi, M., Haberl, F., Jahoda, K., Kaastra, J., Kretschmar, P., Larsson, S., Lubinski, P., Mori, K., Plucinsky, P., Pollock, A. M., Rothschild, R., Sembay, S., Wilms, J., & Yamamoto, M. 2005, in *UV, X-Ray, and Gamma-Ray Space Instrumentation for Astronomy XIV*. Edited by Siegmund, Oswald H. W. *Proceedings of the SPIE*, Volume 5898, pp. 22-33 (2005)., ed. O. H. W. Siegmund, 22–33
- Kubota, A., Dotani, T., Cottam, J., Kotani, T., Done, C., Ueda, Y., Fabian, A. C., Yasuda, T., Takahashi, H., Fukazawa, Y., Yamaoka, K., Makishima, K., Yamada, S., Kohmura, T., & Angelini, L. 2007, *PASJ*, 59, 185
- Kubota, A., Tanaka, Y., Makishima, K., Ueda, Y., Dotani, T., Inoue, H., & Yamaoka, K. 1998, *PASJ*, 50, 667
- Leahy, D. A., Darbro, W., Elsner, R. F., Weisskopf, M. C., Kahn, S., Sutherland, P. G., & Grindlay, J. E. 1983, *ApJ*, 266, 160
- Lee, J. C., Reynolds, C. S., Remillard, R., Schulz, N. S., Blackman, E. G., & Fabian, A. C. 2002, *ApJ*, 567, 1102
- Lund, N., Budtz-Jørgensen, C., Westergaard, N. J., Brandt, S., Rasmussen, I. L., Hornstrup, A., Oxborrow, C. A., Chenevez, J., Jensen, P. A., Laursen, S., Andersen, K. H., Mogensen, P. B., Rasmussen, I., Omø, K., Pedersen, S. M., Polny, J., Andersson, H., Andersson, T., Kämäräinen, V., Vilhu, O., Huovelin, J., Maisala, S., Morawski, M., Juchnikowski, G., Costa, E., Feroci, M., Rubini, A., Rapisarda, M., Morelli, E., Carassiti, V., Frontera, F., Pellicciari, C., Loffredo, G., Martínez Núñez, S., Reglero, V., Velasco, T., Larsson, S., Svensson, R., Zdziarski, A. A., Castro-Tirado, A., Attina, P., Gorla, M., Giulianelli, G., Cordero, F., Rezazad, M., Schmidt, M., Carli, R., Gomez, C., Jensen, P. L., Sarri, G., Tiemon, A., Orr, A., Much, R., Kretschmar, P., & Schnopper, H. W. 2003, *A&A*, 411, L231
- Makishima, K., Maejima, Y., Mitsuda, K., Bradt, H. V., Remillard, R. A., Tuohy, I. R., Hoshi, R., & Nakagawa, M. 1986, *ApJ*, 308, 635
- Mas-Hesse, J. M., Giménez, A., Culhane, J. L., Jamar, C., McBreen, B., Torra, J., Hudec, R., Fabregat, J., Meurs, E., Swings, J. P., Alcacera, M. A., Balado, A., Beiztegui, R., Belenguer, T., Bradley, L., Caballero, M. D., Cabo, P., Defise, J. M., Díaz, E., Domingo, A., Figueras, F., Figueroa, I., Hanlon, L., Hroch, F., Hudcova, V., García, T., Jordan, B., Jordi, C., Kretschmar, P., Laviada, C., March, M., Martín, E., Mazy, E., Menéndez, M., Mi, J. M., de Miguel, E., Muñoz, T., Nolan, K., Olmedo, R., Plessier, J. Y., Polcar, J., Reina, M., Renotte, E., Rochus, P., Sánchez, A., San Martín, J. C., Smith, A., Soldan, J., Thomas, P., Timón, V., & Walton, D. 2003, *A&A*, 411, L261
- Miller, J. M., Raymond, J., Fabian, A. C., Homan, J., Nowak, M. A., Wijnands, R., van der Klis, M., Belloni, T., Tomsick, J. A., Smith, D. M., Charles, P. A., & Lewin, W. H. G. 2004, *ApJ*, 601, 450

- Miller, J. M., Raymond, J., Homan, J., Fabian, A. C., Steeghs, D., Wijnands, R., Rupen, M., Charles, P., van der Klis, M., & Lewin, W. H. G. 2006, *ApJ*, 646, 394
- Mitsuda, K., Inoue, H., Koyama, K., Makishima, K., Matsuoka, M., Ogawara, Y., Suzuki, K., Tanaka, Y., Shibasaki, N., & Hirano, T. 1984, *PASJ*, 36, 741
- Mitsuda, K., Inoue, H., Nakamura, N., & Tanaka, Y. 1989, *PASJ*, 41, 97
- Narita, T., Grindlay, J. E., Bloser, P. F., & Chou, Y. 2003a, *ArXiv Astrophysics e-prints*, 5085, accepted for publication in *ApJ*
- . 2003b, *ApJ*, 593, 1007
- Parmar, A. N., Gottwald, M., van der Klis, M., & van Paradijs, J. 1989a, *ApJ*, 338, 1024
- Parmar, A. N., Oosterbroek, T., Boirin, L., & Lumb, D. 2002, *A&A*, 386, 910
- Parmar, A. N., Oosterbroek, T., Guainazzi, M., Segreto, A., dal Fiume, D., & Stella, L. 1999, *A&A*, 351, 225
- Parmar, A. N., Stella, L., & Giommi, P. 1989b, *A&A*, 222, 96
- Parmar, A. N., White, N. E., Giommi, P., & Gottwald, M. 1986, *ApJ*, 308, 199
- Press, W. H., Rybicki, G. B., & Hewitt, J. N. 1992, *ApJ*, 385, 404
- Retter, A., Chou, Y., Bedding, T. R., & Naylor, T. 2002, *MNRAS*, 330, L37
- Scargle, J. D. 1982, *ApJ*, 263, 835
- Schmidtke, P. C. 1988, *AJ*, 95, 1528
- Sidoli, L., Oosterbroek, T., Parmar, A. N., Lumb, D., & Erd, C. 2001, *A&A*, 379, 540
- Sidoli, L., Parmar, A. N., Oosterbroek, T., & Lumb, D. 2002, *A&A*, 385, 940
- Smale, A. P., Church, M. J., & Bałucińska-Church, M. 2001, *ApJ*, 550, 962
- Smale, A. P., Mason, K. O., White, N. E., & Gottwald, M. 1988, *MNRAS*, 232, 647
- Smale, A. P., Mukai, K., Williams, O. R., Jones, M. H., & Corbet, R. H. D. 1992, *ApJ*, 400, 330
- Titarchuk, L. 1994, *ApJ*, 434, 570
- Ubertini, P., Lebrun, F., Di Cocco, G., Bazzano, A., Bird, A. J., Broenstad, K., Goldwurm, A., La Rosa, G., Labanti, C., Laurent, P., Mirabel, I. F., Quadriani, E. M., Ramsey, B., Reglero, V., Sabau, L., Sacco, B., Staubert, R., Vigroux, L., Weisskopf, M. C., & Zdziarski, A. A. 2003, *A&A*, 411, L131

- Ueda, Y., Murakami, H., Yamaoka, K., Dotani, T., & Ebisawa, K. 2004, *ApJ*, 609, 325
- van der Klis, M., Jansen, F., van Paradijs, J., & Stollmann, G. 1985, *Space Science Reviews*, 40, 287
- Vedrenne, G., Roques, J.-P., Schönfelder, V., Mandrou, P., Lichti, G. G., von Kienlin, A., Cordier, B., Schanne, S., Knödlseider, J., Skinner, G., Jean, P., Sanchez, F., Caraveo, P., Teegarden, B., von Ballmoos, P., Bouchet, L., Paul, P., Matteson, J., Boggs, S., Wunderer, C., Leleux, P., Weidenspointner, G., Durouchoux, P., Diehl, R., Strong, A., Cassé, M., Clair, M. A., & André, Y. 2003, *A&A*, 411, L63
- Walter, F. M., Mason, K. O., Clarke, J. T., Halpern, J., Grindlay, J. E., Bowyer, S., & Henry, J. P. 1982, *ApJ*, 253, L67
- Warwick, R. S., Marshall, N., Fraser, G. W., Watson, M. G., Lawrence, A., Page, C. G., Pounds, K. A., Ricketts, M. J., Sims, M. R., & Smith, A. 1981, *MNRAS*, 197, 865
- White, N. E., Stella, L., & Parmar, A. N. 1988, *ApJ*, 324, 363
- White, N. E., & Swank, J. H. 1982, *ApJ*, 253, L61
- Winkler, C., Courvoisier, T. J.-L., Di Cocco, G., Gehrels, N., Giménez, A., Grebenev, S., Hermsen, W., Mas-Hesse, J. M., Lebrun, F., Lund, N., Palumbo, G. G. C., Paul, J., Roques, J.-P., Schnopper, H., Schönfelder, V., Sunyaev, R., Teegarden, B., Ubertini, P., Vedrenne, G., & Dean, A. J. 2003, *A&A*, 411, L1
- Xiang, J., Lee, J. C., & Nowak, M. A. 2007, *ApJ*, 660, 1309

Table 1: Properties of the studied LMXBs. L_{36} is the 0.6–10 keV luminosity in units of 10^{36} erg s $^{-1}$ for distances d taken from Díaz Trigo et al. (2006), except for XB 1323–619 where the 0.5–10 keV luminosity is from Boirin et al. (2005). $N_{\text{H}}^{\text{xabs}}$ is the persistent and dipping emission column density in units of 10^{22} atom cm $^{-2}$ of the best-fit photo-ionized absorber with an ionization parameter $\log(\xi)$ (in units of erg cm s $^{-1}$) measured by XMM-Newton (Boirin et al. 2005; Díaz Trigo et al. 2006). Note that no such absorber was required with the fits to 4U 1746–371 (Díaz Trigo et al. 2006).

LMXB	P_{dip} (hr)	L_{36} (erg s $^{-1}$)	d (kpc)	$N_{\text{H}}^{\text{xabs}}$		$\log(\xi)$		P_{dip} Reference
				Non-dip / Dip	Non-dip / Dip	Non-dip / Dip	Non-dip / Dip	
XB 1916–053	0.833351411(25)	4.4	9.3	$4.2^{+0.5}_{-0.5} / 28^{+2}_{-2}$	$3.05^{+0.04}_{-0.04} / 2.55^{+0.04}_{-0.04}$	Chou et al. (2001)		
XB 1323–619	2.94(2)	5.2	10	$3.8^{+0.4}_{-0.4} / 14^{+10}_{-7}$	$3.9^{+0.04}_{-0.04} / 3.0^{+0.2}_{-0.2}$	Bałucińska-Church et al. (1999)		
4U 1746–371	5.16(1)	10.1	10.7	Bałucińska-Church et al. (2004)		
X 1624–490	20.8778(3)	47.5	15	$13^{+2}_{-0.4} / 29^{+4}_{-4}$	$3.6^{+0.2}_{-0.2} / 3.0^{+0.2}_{-0.2}$	Smale et al. (2001)		

Table 2: Observation Log. The longer exposure times for ISGRI compared with JEM-X are due to the larger FOV of this instrument. Mean count rates are given in the energy range 4.0–20 keV for JEM-X and 20–200 keV for ISGRI.

LMXB	Exposure (ks)		Count Rate (s $^{-1}$)		Tstart-Tstop (MJD)	
	JEM-X	ISGRI	JEM-X	ISGRI	JEM-X	ISGRI
XB 1916–053	293	915	3.5	1.2	52952.4-52963.5	52708.7-53310.6
XB 1323–619	497	834	0.96	0.66	53085.7-53263.9	52650.7-53263.9
4U 1746–371	316	626	6.4	0.43	52713.4-53068.1	52713.3-53292.7
X 1624–490	398	756	9.4	0.42	52701.8-53062.0	52700.7-53265.2

Table 3: A summary of modulation depths for the dipping LMXBs analyzed in this work. The depths are given in percentage modulation normalized to mean count rate ($\sim 100 \times (\text{max rate} - \text{min rate}) / (\text{max rate} + \text{min rate}) / 2$).

LMXB	3-10 keV	20-40 keV	40-100 keV
XB 1916–053	18%	25%	<15%
XB 1323–619	40%	<14%	–
4U 1746–371	<10%	45%	–
X 1624–490	25%	40%	–

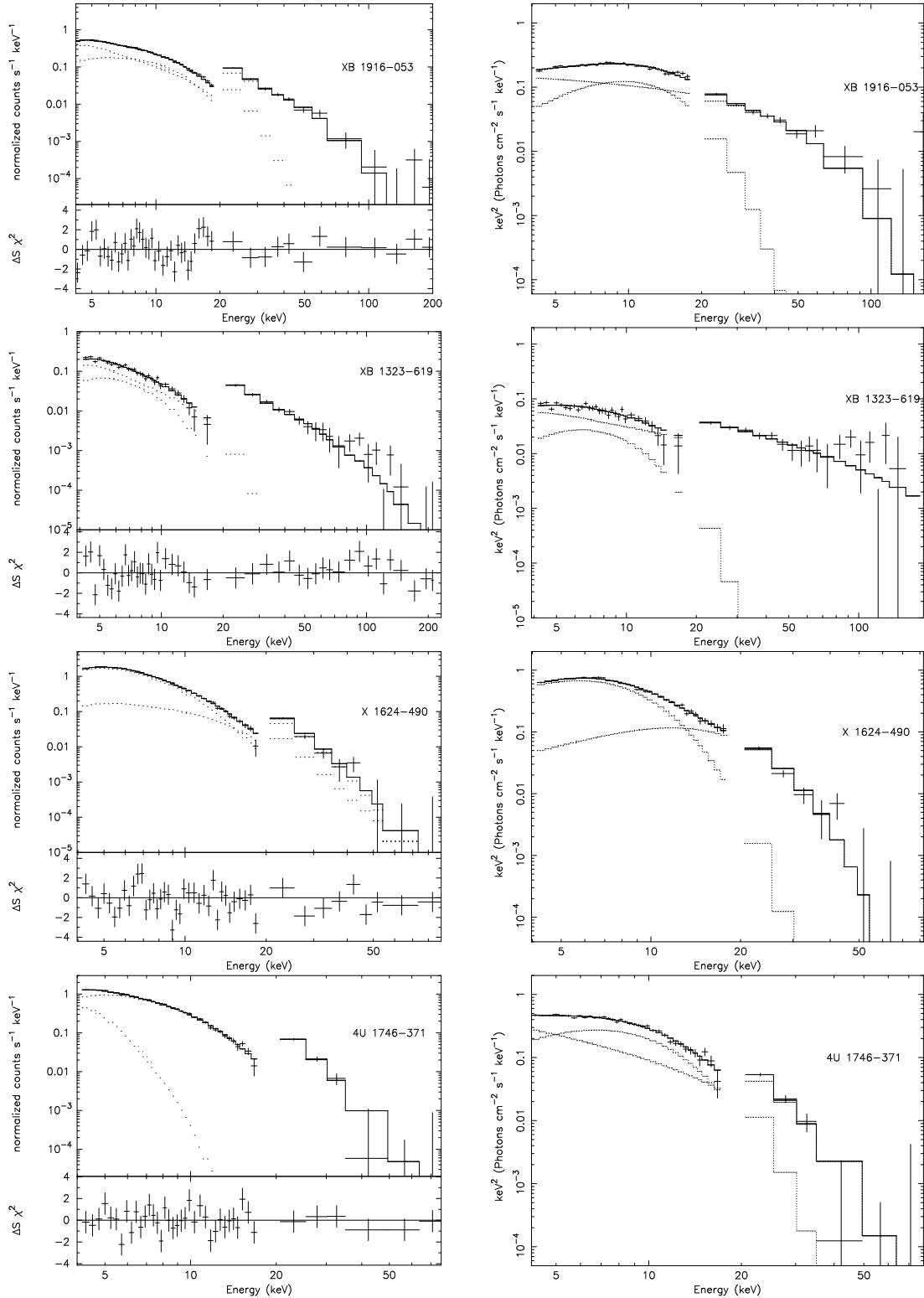


Fig. 6.— Simultaneous 4–200 keV fits to the JEM-X and ISGRI spectra of the four dipping LMXBs (4–20 keV; JEM-X and 20–200 keV; ISGRI). The crosses indicate the data, the solid lines show the summed model and the dotted lines show the individual models. The second panel under each count rate spectra display the residuals in standard deviations. Next to each count rate spectrum an unfolded spectrum in E^2F is plotted to show the contribution of each component of the spectrum.

Table 4: Best-fit spectral parameters obtained using a cutoff power-law or compTT model together with either a disk blackbody or blackbody component. N_{H} is the absorbing column in units of 10^{22} atom cm^{-2} , kT is the blackbody or disk blackbody temperature in keV, K_{D} and K_{B} are the normalisations of the disk blackbody and blackbody models, Γ is the power law photon index, E_{cut} is the cutoff energy in keV, K_{cut} is the model normalisation photon $\text{cm}^{-2} \text{s}^{-1} \text{keV}^{-1}$ at 1 keV, F is the 4–200 keV flux in units of 10^{-10} erg $\text{cm}^{-2} \text{s}^{-1}$ and L is the 4–200 keV source luminosities at the distances given in Table 1 in units of 10^{36} erg s^{-1} , kT_0 is the input soft photon (Wien) temperature (keV), kT_{P} is the plasma temperature (keV) and τ is the plasma optical depth (electron scattering opacity).

Model	Disk Blackbody + Cutoff Power-law				Blackbody + Cutoff Power-law			
	XB 1916–053	XB 1323–619	X 1624–490	4U 1746–371	XB 1916–053	XB 1323–619	X 1624–490	4U 1746–371
N_{H}	0.4 (<2.9)	3.5 (<3.9)	$2.9^{+4.5}_{<}$	0.4 (<1.3)	0.4 (<5.2)	3.5 (<5.0)	$3.5^{+3.6}_{-1.9}$	0.4 (<3.1)
kT	$3.5^{+0.2}_{-0.2}$	$2.3^{+0.4}_{-0.2}$	$3.4^{+0.4}_{-0.3}$	$2.3^{+0.1}_{-0.2}$	$2.4^{+0.1}_{-0.1}$	$1.7^{+0.3}_{-0.2}$	$1.4^{+0.1}_{-0.1}$	$1.7^{+0.1}_{-0.1}$
K_{D}	$0.14^{+0.04}_{-0.03}$	$0.5^{+0.9}_{-0.4}$	$0.3^{+0.3}_{-0.2}$	$7.4^{+3.1}_{-2.4}$				
K_{B}					$0.004^{+0.001}_{-0.001}$	$0.0018^{+0.0014}_{-0.0011}$	$0.02^{+0.008}_{-0.005}$	$0.019^{+0.003}_{-0.005}$
Γ	$1.7^{+0.3}_{-0.3}$	$2.9^{+0.2}_{-0.2}$	$-2.0^{+0.5}_{-0.7}$	$2.4^{+0.3}_{-0.2}$	$2.1^{+0.3}_{-0.3}$	$3.0^{+0.1}_{-0.2}$	$0.2^{+0.7}_{-1.5}$	$2.2^{+0.7}_{-0.8}$
E_{cut}	$26.7^{+5.2}_{-3.4}$	$199.30^{<}_{90.00}$	$1.3^{+0.2}_{-0.1}$	$9.4^{+2.0}_{-1.2}$	$26.0^{+7.5}_{-5.0}$	$500.00^{<}_{390.00}$	$4.1^{+0.5}_{-0.5}$	$6.74^{+4.5}_{-2.2}$
K_{cut}	$0.05^{+0.03}_{-0.02}$	$0.6^{+0.4}_{-0.3}$	$0.07^{+0.04}_{-0.02}$	$0.8^{+0.3}_{-0.3}$	$0.2^{+0.1}_{-0.1}$	$0.9^{+0.6}_{-0.4}$	$0.044^{+0.013}_{-0.013}$	$2.2^{+2.3}_{-1.2}$
F	5.7	1.8	20.7	9.5	6.9	1.9	12.4	8.5
L	5.6	2.2	56.2	13.1	6.7	2.3	33.7	11.8
χ^2_{ν} (dof)	1.3 (42)	1.2 (47)	1.34 (41)	1.1 (34)	1.4 (42)	1.2 (42)	1.4 (40)	1.14 (36)

Model	Disk Blackbody + CompTT				Blackbody + CompTT			
	XB 1916–053	XB 1323–619	X 1624–490	4U 1746–371	XB 1916–053	XB 1323–619	X 1624–490	4U 1746–371
N_{H}	0.4 (< 1.2)	3.5 (<6.4)	$3.0^{+1.6}_{-1.6}$	0.4 (<1.3)	0.4 (<3.1)	3.5 (<3.6)	$3.1^{+0.1}_{-0.1}$	0.4 (<12.0)
kT	$3.6^{+0.2}_{-0.2}$	$2.3^{+0.4}_{-0.3}$	$3.4^{+0.4}_{-0.2}$	$2.3^{+0.1}_{-0.2}$	$2.44^{+0.10}_{-0.10}$	$1.7^{+0.3}_{-0.2}$	$1.4^{+0.1}_{-0.1}$	$0.6^{+0.1}_{-0.1}$
K_{D}	$0.14^{+0.04}_{-0.05}$	$0.5^{+0.7}_{-0.4}$	$0.3^{+0.1}_{-0.3}$	$7.5^{+2.9}_{-1.8}$				
K_{B}					$0.0048^{+0.0003}_{-0.0002}$	$0.0014^{+0.0008}_{-0.0007}$	$0.025^{+0.002}_{-0.002}$	$0.04^{+0.02}_{-0.01}$
kT_0	$0.7^{+0.3}_{-0.6}$	$0.4^{+0.3}_{-0.3}$	$1.3^{+2.2}_{-0.2}$	$0.4^{+0.8}_{-0.3}$	$0.7^{+0.1}_{-0.2}$	$0.4^{+0.2}_{-0.3}$	$2.5^{+0.3}_{-0.2}$	$1.6^{+0.1}_{-0.1}$
kT_{P}	$12.3^{+5.2}_{-2.9}$	$239.5^{+34.4}_{-47.6}$	$11.9^{+3.4}_{-3.1}$	$4.8^{+7.8}_{-1.7}$	$18.8^{+10.9}_{-6.0}$	$196.4^{+28.5}_{-18.8}$	$9.2^{+2.5}_{-1.9}$	$4.9^{+5.6}_{-1.9}$
τ_{P}	$2.1^{+0.8}_{-1.0}$	$0.003^{+0.002}_{-0.002}$	$0.0038^{+0.0030}_{-0.0030}$	$2.6^{+3.7}_{-2.4}$	$0.9^{+0.7}_{-0.6}$	$0.006^{+0.001}_{-0.004}$	$0.22^{+4.21}_{-0.20}$	$1.1^{+2.3}_{-0.9}$
K_{C}	$0.003^{+0.013}_{-0.002}$	$0.0010^{+0.064}_{-0.0007}$	$0.03^{+0.1}_{-0.01}$	$0.10^{+2.92}_{-0.08}$	$0.005^{+0.003}_{-0.003}$	$0.0008^{+0.0120}_{-0.0005}$	$0.006^{+0.001}_{-0.001}$	$0.11^{+0.10}_{-0.10}$
F	5.8	1.8	12.7	9.0	5.9	3.3	21.6	11.0
L	5.7	2.2	34.5	12.4	5.7	4.0	58.7	15.2
χ^2_{ν} (dof)	1.3 (41)	1.2 (42)	1.4 (40)	1.3 (35)	1.4 (41)	1.3 (42)	1.4 (40)	1.1 (35)

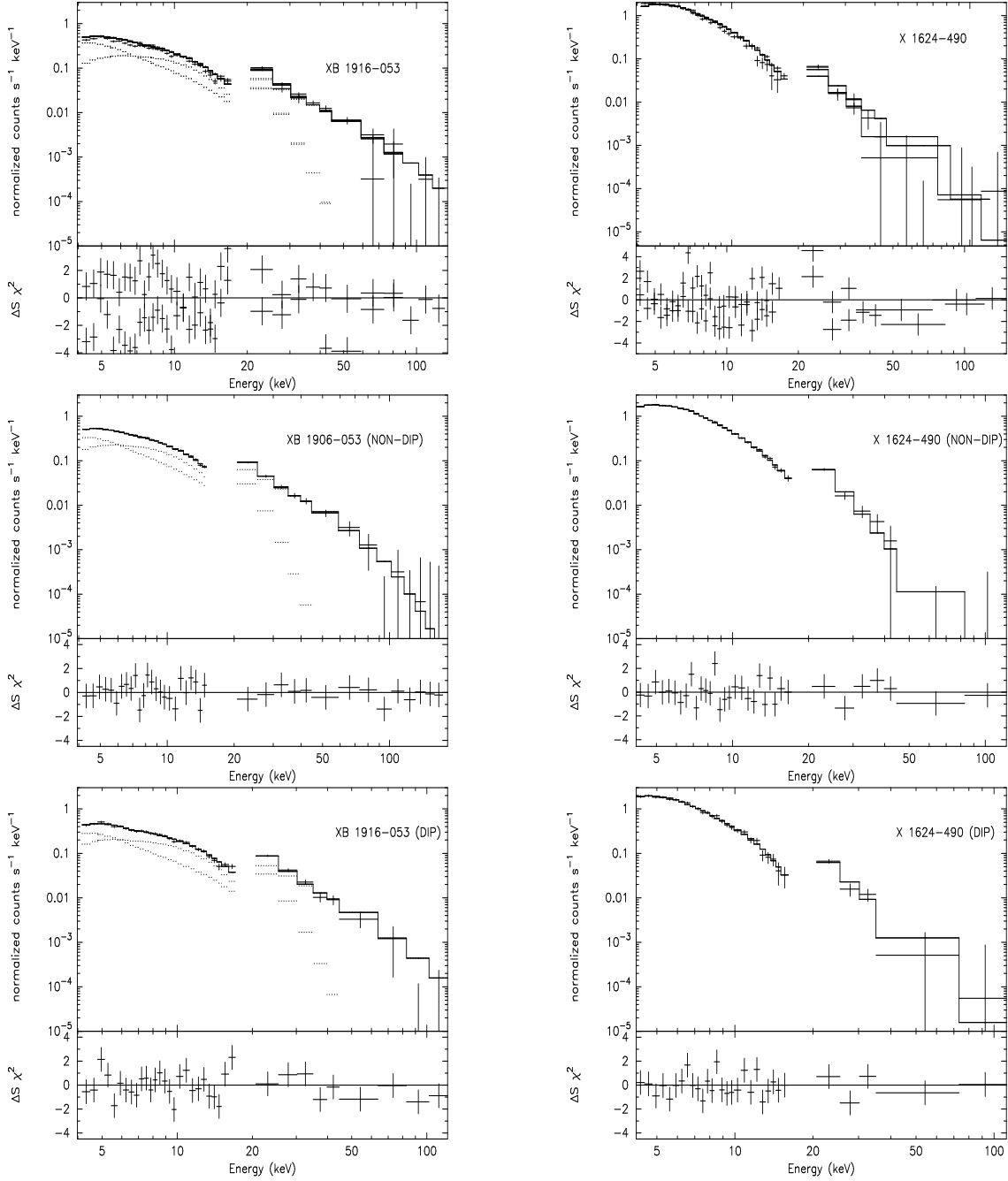


Fig. 7.— Simultaneous 4–200 keV fits to the JEM-X and ISGRI time-average spectra of XB 1916–053 (left) and X 1624–490 (right) (4–20 keV; JEM-X and 20–200 keV; ISGRI). Crosses indicate the data, the solid lines show the summed model and the dotted lines show the individual models. The second panel under each count rate spectra display the residuals in standard deviations. The top panels are dip and non-dip spectra fitted simultaneously with only the blackbody and `compTT` model (`wabs*(bbody+compTT)`). The middle and bottom panels are non-dip and dip spectra, respectively, fitted with the composite model including the warm absorber model (`wabs*warmabs*(bbody+compTT)`).